



# The angular dislocation parallel to a free surface. Application to a (111)Si low angle twist boundary

Salem Neily, Sami Youssef, Frank Fournel, R. Bonnet

## ► To cite this version:

Salem Neily, Sami Youssef, Frank Fournel, R. Bonnet. The angular dislocation parallel to a free surface. Application to a (111)Si low angle twist boundary. Philosophical Magazine, 2011, 91 (31), pp.1. 10.1080/14786435.2011.600734 . hal-00723598

**HAL Id: hal-00723598**

**<https://hal.science/hal-00723598>**

Submitted on 11 Aug 2012

**HAL** is a multi-disciplinary open access archive for the deposit and dissemination of scientific research documents, whether they are published or not. The documents may come from teaching and research institutions in France or abroad, or from public or private research centers.

L'archive ouverte pluridisciplinaire **HAL**, est destinée au dépôt et à la diffusion de documents scientifiques de niveau recherche, publiés ou non, émanant des établissements d'enseignement et de recherche français ou étrangers, des laboratoires publics ou privés.



**The angular dislocation parallel to a free surface.  
Application to a (111)Si low angle twist boundary**

Journal:	<i>Philosophical Magazine &amp; Philosophical Magazine Letters</i>
Manuscript ID:	TPHM-11-Mar-0097.R1
Journal Selection:	Philosophical Magazine
Date Submitted by the Author:	09-Jun-2011
Complete List of Authors:	Bonnet, R.; INP Grenoble, SIMAP (ex LTPCM) NEILY, Salem; Unité de recherche de Physique du Solide,, Faculté des Sciences de Monastir, Youssef, Sami; Faculté des Sciences de Monastir, Unité de Recherche Physique des Solides fournel, frank; CEA-DRT-LETI-CEA/GRE, Centre d'Etude Atomique
Keywords:	dislocation theory, thin films, electron microscopy, silicon
Keywords (user supplied):	interface

SCHOLARONE™  
Manuscripts

**The angular dislocation parallel to a free surface. Application to a (111)Si low angle twist boundary**

S. Neily<sup>†</sup>, S. Youssef<sup>†</sup>, F. Fournel<sup>††</sup> and R. Bonnet<sup>†††</sup>

<sup>†</sup> Unité de recherche de Physique du Solide, Faculté des Sciences de Monastir, Boulevard de l'Environnement, Université de Monastir, 5019 Monastir, Tunisie

<sup>††</sup> CEA, LETI, MINATEC, F-38054 Grenoble, France

<sup>†††</sup> SIMAP, INPGrenoble-CNRS-UJF, Domaine Universitaire, BP1 75, 38402 Saint Martin d'Hères, France

**Abstract**

The elastic displacement field of a sharply angular dislocation with its two legs parallel to a planar free surface is given in a practical analytical form. Its expression gives access, in transmission electron microscopy (TEM), to computed images of numerous interacting dislocations all located at a distance  $h$  close to the free surface. As an application, this field is used repeatedly to study, in dark-field TEM and a  $g(3g)$  diffraction mode with  $g\{220\}$ , the contrast of dissociated triple nodes of a low-angle twist boundary in silicon extended over a (111) plane. It is shown that free surface elastic effects can influence the contrasts of some  $30^\circ$  partials if  $h$  is at nanometer scale.

Keywords : dislocation theory, elasticity, interface, silicon, transmission electron microscopy

**1. Introduction**

There are two main ways to evaluate the elastic field of a general dislocation in an elastic isotropic solid limited by a planar free surface. The first one is to perform an integration of expressions giving the displacement field  $\mathbf{u}$  of an infinitesimal loop [1] over an appropriate spatial domain, while the second way uses repeatedly the concept of a sharply angular dislocation introduced by Yoffe [2,3]. For a semi-infinite medium, two particular dislocations have known algebraical  $\mathbf{u}$  fields. They are illustrated in figure 1 : (i) an inclined straight dislocation [3] piercing the surface in K, with Burgers vector  $\mathbf{b}_1$ , and (ii), a sharply angular dislocation [4] with a Burgers vector  $\mathbf{b}_2$ . This latter has a line geometry such that one semi-infinite leg OH is perpendicular to the free surface (P), while the other leg makes an angle  $\beta \leq \pi/2$ . For

simplicity, dislocations  $\mathbf{b}_1$  and  $\mathbf{b}_2$  are denoted below as " Yoffe " and " Comninou " dislocations respectively.

The  $\mathbf{u}$  field of a Comninou dislocation is calculated in [4] from the superposition, in an infinite medium, of three different elastic fields. The superposition is appropriately chosen so as to generate a plane along which there are no applied forces, i. e., the chosen plane (P) of the free surface. The three fields in question are those of two angular dislocations in an infinite medium with their lines located symmetrically with respect to the plane (P), plus a third complementary field required to cancel the non-zero stresses along (P). As already noted in [4], the combination of these two particular dislocations is useful to determine explicitly, in a semi-infinite medium, the  $\mathbf{u}$  field of any dislocation line formed by finite and/or semi-infinite segments. The results obtained in [2-4] have been checked numerically and some typographical errors were corrected in [5]. In what follows, symbols and notations are the same as those presented in this latter reference.

The present work has two parts. Firstly, it is shown that if a sharply angular dislocation has no legs perpendicular to the surface, the expression of its  $\mathbf{u}$  field can be greatly simplified and will therefore be of easy use for numerical applications. Secondly, using this expression, a transmission electron microscopy (TEM) investigation of a low angle twist boundary in silicon is presented. The corresponding dislocation network, which is extended over a (111) plane, has been fabricated by hydrophobic molecular bonding after twisting a (111)Si ultra thin crystal by  $0.16^\circ$  with respect to a (111)Si substrate. The technology producing such bicrystals, quite similar to that largely described in the past for the (001) interface, see e. g. [6,7], is not commented below.

## 2. The $\mathbf{u}$ field of an angular dislocation parallel to a surface.

Figure 2 describes the construction of the elastic field of an angular dislocation parallel to a surface (ADPS) with a Burgers vector  $\mathbf{b}$ . It is constructed from the superposition of two Comninou dislocations oriented TOU (Burgers vector  $\mathbf{b}$ ) and QOU (Burgers vector  $-\mathbf{b}$ ). These two latter dislocations, placed at distance  $h$  from the surface, have legs OT and OQ making the angle  $\alpha$  between them. Therefore, the final elastic field results from the addition of four Yoffe dislocations and two complementary elastic fields.

At first sight, when looking at these expressions that spread over a number of journal pages, it seems intractable to handle them in the hope of simplifying them. However, taking into account of the  $\pi/2$  apex angle of the two Comninou dislocations and of tedious simplifications, it was found possible to reduce the sum of these six elastic fields into a compact, practical, analytic form. In the Cartesian frame Oxyz for which Oy//OT and Oz//OU, the displacement field of dislocation TOU is, with the summation convention on repeated indices,

$$u_k = K f_{ki} b_i, \quad (i, k = 1 \text{ to } 3) \quad (1)$$

in which

$$K = 1/(8\pi(1-\nu)), \quad (2)$$

$b_i$  are the components of the Burgers vector,

the nine functions  $f_{ki}$  depend on  $x, y, z$ .

With

$$r = \sqrt{x^2 + y^2 + z^2}, \quad (3)$$

$$Z = z + 2h, \quad (4)$$

$$R = \sqrt{x^2 + y^2 + Z^2}, \quad (5)$$

$$F = -2 \operatorname{Arctan}(-x/y) + \operatorname{Arctan}(x/z) + 2 \operatorname{Arctan}((rx)/(yz)) + \operatorname{Arctan}(-x/Z) + \operatorname{Arctan}((-Rx)/(yZ)), \quad (6)$$

the functions  $f_{ki}$  are the following

$$\begin{aligned} f_{11} = & x \left( \frac{z}{r^2 - ry} + \frac{y}{r^2 - rz} + \frac{y}{R^2 + RZ} - \frac{Z}{R^2 - Ry} \right) - 2F(1-\nu) \\ & + 2x \left( \frac{hZ(2R-y)(h+z)}{R^3(R-y)^2} + \frac{y(1-2\nu)}{(R+Z)^2} \left( \frac{h}{R} + \nu \right) - \frac{h(1-2\nu)}{R^2 - Ry} - \frac{y(h+z)(h(2R+Z) + 2\nu R^2)}{R^3(R+Z)^2} \right); \\ f_{12} = & (1-2\nu) \left( \operatorname{Log}(r-z) + (1-2\nu) \operatorname{Log}(R+Z) \right) - x^2 \left( \frac{1}{r^2 - rz} + \frac{1}{R^2 + RZ} \right) \\ & + \frac{2(1-2\nu)}{R+Z} \left( h - \nu Z - \frac{x^2}{R+Z} \left( \frac{h}{R} + \nu \right) \right) + \frac{2(h+z)}{R+Z} \left( \frac{hx^2}{R^3} - \frac{h}{R} - 2\nu + \frac{x^2(h+2\nu R)}{R^2(R+Z)} \right); \\ f_{13} = & \frac{2(h+z)}{R^3} \left( h \left( y + \frac{Z^2(y-2R)}{(R-y)^2} \right) + R^2 \left( \frac{Z}{y-R} + \frac{y}{Z+R} \right) \right) + \frac{2h(h+z) - x^2(3-4\nu)}{R(R-y)} + \frac{x^2}{r(y-r)} \\ & - 2(1-2\nu) \left( \frac{Z^2(x^2 + zZ)}{(x^2 + Z^2)^2} - \frac{y(y^2z + x^2Z)}{(x^2 + y^2)^2} + \frac{h}{R^3} \left( \frac{Rx^2y}{(R+Z)^2} - \frac{y(y^2 + Z^2)}{Z+R} + \frac{Z(R^3 - 2Rx^2 - y^3 - yZ^2)}{(R-y)^2} \right) \right) \\ & + yZ \left( \frac{2hx^2(R^2 + x^2)^2}{R(R^2x^2 + y^2Z^2)^2} + \frac{hx^2(x^2 - 3R^2) + zR^2(R^2 + x^2)}{R^3(R^2x^2 + y^2Z^2)} \right) + \frac{1}{2} \operatorname{Log} \left( \frac{R-y}{r-y} \right) \\ f_{21} = & \frac{Z}{R} - \frac{z}{r} + y^2 \left( \frac{1}{r^2 - rz} + \frac{1}{R^2 + RZ} \right) + \frac{2h}{R} \left( 1 - 2\nu - \frac{Z(h+z)}{R^2} \right) + \frac{2(1-2\nu)}{R+Z} \left( Z\nu - h + \frac{y^2}{R+Z} \left( \frac{h}{R} + \nu \right) \right) \\ & + \frac{2(h+z)}{R+Z} \left( \frac{h}{R} - \frac{hy^2}{R^3} + 2\nu - \frac{y^2(h+2\nu R)}{R^2(R+Z)} \right) - (1-2\nu) \left( \operatorname{Log}(r-z) + (1-2\nu) \operatorname{Log}(R+Z) \right) \end{aligned}$$

$$f_{22} = \frac{2x y (h R(z + Z - R) + h Z(h + z) + v R^2(2Z - R) + 2v^2 R^3)}{R^3(R + Z)^2} - x y \left( \frac{1}{r^2 - r z} + \frac{1}{R^2 + R Z} \right) - 2F(1 - v);$$

$$f_{23} = \frac{x}{R^3} \left( \frac{4(1 - v) R^2(h + R)}{R + Z} + \frac{R^2(R - r)}{r} - 2h(h + z) \right);$$

$$f_{31} = (1 - 2v) \text{Log} \left( \frac{R - y}{r - y} \right) + \frac{1}{R} \left( y + \frac{Z^2}{y - R} \right) - \frac{1}{r} \left( y + \frac{z^2}{y - r} \right) - \frac{4(1 - v)}{R} \left( \frac{y(h + 2v R)}{R + Z} - \frac{h Z}{R - y} \right) \\ + \frac{2}{R^3} \left( \frac{h(h + z)}{(R - y)^2} \left( (y - R)(x^2 + y^2) + R Z^2 \right) - y(h + z) \left( h + \frac{2v R^2}{R + Z} \right) \right);$$

$$f_{32} = x \left( \frac{1}{r} - \frac{1}{R} \right) + \frac{2x}{R} \left( \frac{2(1 - v)(h + 2v R)}{(R + Z)} + (h + z) \left( \frac{h}{R^2} + \frac{2v}{R + Z} \right) \right);$$

$$f_{33} = \frac{x(Z + 2h(1 - 2v))}{R(R - y)} - \frac{x z}{r^2 - r y} + \frac{2h x Z(Z - h)}{R^2(R - y)} \left( \frac{1}{R} + \frac{1}{R - y} \right) - 2F(1 - v).$$

The elastic displacement field of QOU can also be expressed relative to Oxyz. The same functional form as the expression of equation (1) describes this field in the axis system Ox'y'z', i. e.,  $\mathbf{u}(x', y', z', \mathbf{b}')$ . It is obtained from by substitution of the variables  $x, y, z$  into  $x', y', z'$  and the change of  $\mathbf{b}$  into  $\mathbf{b}'$ . From the matrix

$$M = \begin{bmatrix} \cos \alpha & -\sin \alpha & 0 \\ \sin \alpha & \cos \alpha & 0 \\ 0 & 0 & 1 \end{bmatrix}, \quad (7)$$

the elastic field of dislocation QOU in Oxyz is expressed by

$$M \cdot \mathbf{u}(x', y', z', \mathbf{b}'), \quad (8)$$

in which

$$\{x', y', z'\} = M^{-1} \cdot \{x, y, z\}, \quad (9)$$

$$\mathbf{b}' = M^{-1} \cdot (-\mathbf{b}). \quad (10)$$

The sum of expressions (1) and (8) gives therefore the displacement field of the ADPS. If  $\alpha = \pi$ , we have to do with a straight dislocation parallel to the surface. The corresponding elastic field has been checked numerically relative to the elastic field given for the edge [8] and screw cases [9]. Another check was done for an ADPS located far from the surface : expression (1) tends to the same elastic field as that of an

angular dislocation in an infinite medium [4]. The conditions of zero applied force along the free surface and the equilibrium equations of classical elasticity were verified numerically.

3. TEM contrast of dissociated nodes in a low angle twist boundary in silicon.

An application of the above expressions has been performed to examine if the TEM dark-field technique, usually adopted to analyse dislocation configurations in the thinner part of thin foils, could be sensitive to elastic relaxation due to a nearby free surface. A silicon bicrystal containing a low angle twist boundary extended on a (111) plane was prepared from hydrophobic wafer bonding at room temperature of two distinct (111) wafers (p doped wafers with resistivity between 1-20  $\Omega/\text{cm}$ ). An anneal above 1000°C gives a stable interface structure, see e.g. [6,7]. The technological process is able to control the twist angle at a precision better than 0.01°. A twist angle  $\psi \approx 0.16^\circ$  was selected to observe clearly well separated nodes of the hexagonal dislocation network. The original preparation technique of the bicrystal allows us also to drastically minimize the tilt misorientation and the associated edge dislocation array. This allows the creation of an almost pure twist boundary. The bicrystal is formed at room temperature by simple adhesion of an ultrathin film with a 25 nm thickness deposited on a (111) wafer substrate followed by an anneal at high temperature. The thickness is controlled by indirect ellipsometry measurement [6,7]. Figure 3 is a schematic diagram depicting a cross section of a thin foil : the specimen is thinned towards the substrate side in order to keep unchanged the film thickness, except of course near the edge of the foil. In regions nearby the edge of the foil, the substrate thickness is denoted  $h$  in the expression of the  $f_{ki}$ ;  $h$  can reach a zero value. Particular contrasts are therefore expected in these regions. The expressions written above are applied with a normal  $\mathbf{N}$  directed from the layer to the substrate side.

3.1 Bright field imaging with a many-beam diffraction mode.

Figure 4 is a many-beam bright field image taken with an electron beam very close to [111], see e.g. the diffraction pattern inserted in figure 4. The average period of the hexagonal network is in agreement with the Frank formula, close to 137 nm. White arrows indicate two alternating intrinsic-extrinsic nodes. These nodes are connected by a black, near horizontal, contrast in the form of a thin corridor that opens gradually from the left hand side arrow to the other arrow. This peculiarity of the contrast can be observed everywhere in the figure, except in the middle where the black contrast is much shorter. This observation shows that the junction between the two faults can be instable. As already observed in [10] for an interface with a twist angle  $\psi \approx 0.4^\circ$  presenting a much higher dislocation density, the interface geometry is that of a hexagonal pattern with alternating intrinsic and extrinsic nodes. Neither precipitates could be detected in the present interface nor double-ribbons of faults, a situation still observed in [10]. Similar

intrinsic-extrinsic nodes of hexagonal dislocation networks, were also observed in an Ag-In alloy [11], at the Si-Ge interface [12], and for a subsurface dislocation network generated by the annealing of a (111)Ni<sub>75</sub>Pt<sub>25</sub> single crystal [13,14].

To improve the imaging condition of the nodes, dark-field images were performed and regions of the thin foil for which the substrate thickness is only a few nanometers were preferentially selected. The imaging condition uses dark-field transmission electron microscopy at 300 kV [15-17]. The computer program uses an algorithm similar to those described in [18,19]. The Thompson tetrahedron [20] is represented in some figures in a convenient orientation to help the description of the Burgers vectors.

### 3.2 Dark-field imaging with a $g(3g)$ diffraction mode of the bicrystal.

The interpretation of the contrasts is based on many-beam image simulations for a specimen tilted around reciprocal rows  $g\{220\}$ , using a systematic reciprocal row only, and a zero value for the deviation from the Bragg reflection on  $3g$ . It is called a  $g(3g)$  diffraction mode [17].

The deviation parameters corresponding to the diffracted beams are the same than those calculated as in [19]. For a wave length equal to  $\lambda = 0.197 \text{ nm}$ ,  $s_g = -0.107 \text{ nm}^{-1}$ ,  $s_g = s_{2g} = +0.0535 \text{ nm}^{-1}$  and  $s_{3g} = 0$ . The extinction distances are also those adopted in [19] :  $\xi_g = 110.3 \text{ nm}$ ,  $\xi_{2g} = 322.4 \text{ nm}$  and  $\xi_{3g} = 566.6 \text{ nm}$ . The anomalous absorption parameters are the same :  $A_g = 0.091$ , and  $A_{2g} = A_{3g} = 0.12$ . The Poisson ratio is 0.218 [9] and the lattice parameter is 0.54282 nm [21]. Three different orientations of the specimen were selected, with electron beams  $\mathbf{B}$  very close to [558], [535] and [855]. The example of an image taken with  $\mathbf{B} \approx [855]$  and  $g(02\bar{2})$  is shown in figure 5, which includes the corresponding diffraction pattern and four diffracted beams. Because of the orientation of the crystal (see the Thompson tetrahedron), the node at the left hand side of the white arrow is necessarily an extrinsic node, the three nodes around it being extended intrinsic nodes. This geometric property, easy to check, was also used in [9] to identify the nature of the stacking faults and the Burgers vectors. Figure 6 describes the Burgers vectors of the partial dislocations related to an extrinsic node.

Figure 7 depicts the geometric model adopted for the contrast simulation of this node in terms of 12 ADPS (description in §2). The extrinsic fault is a truncated triangle, with very short lines of partial dislocations with Burgers vectors  $\mathbf{A}\delta$ ,  $\delta\mathbf{C}$  and  $\mathbf{B}\delta$  bordering three narrow corridors of intrinsic faults extending beyond segments MN, PQ and RS. The Cartesian system  $OX_1X_2X_3$  associated to the screen is such that O is the projected centre of the regular truncated triangle lying in the (111) plane, the geometry of which respects the 3-fold symmetry and symmetry with respect to orientations  $\langle 110 \rangle$  of this plane. The axis  $OX_3$  is oriented upwards, along the projected direction of  $\mathbf{BA}$  onto the screen. The axis  $OX_2$  is the integration direction along the optical axis oriented  $-\mathbf{B}$ . In this schematic diagram, the superposed



dislocation segments are artificially made visible with very close and parallel lines. The very slight curvatures of the partial dislocations limiting the intrinsic faults is therefore neglected near M, N, P, Q, R and S. So, the geometry of the node is completely specified by three parameters : the distance  $L$  of point O to segments RQ, SM and NP ; the length  $S$  of the small segments MN, PQ and RS ; the orientations of the 12 semi-infinite dislocation branches which limit the three surrounding intrinsic faults, orientations close to  $\langle 110 \rangle$  directions. Because of the symmetry of the figure, the orientations of all these branches are fixed by the small angle  $\varepsilon$  between vectors  $\mathbf{BA}$  and  $\mathbf{nN}$ .

For numerical application, an image taken with  $\mathbf{B} = [558]$  and  $\mathbf{g}(\bar{2}20)$  was chosen for which the substrate thickness reaches a zero value. This condition reveals clearly the dissociation of the screw dislocations  $\mathbf{BA}$ . Figure 8 exhibits regions where some dislocation segments were removed during the thinning preparation or escape to the free surface. The lower part of the experimental image exhibited in figure 9(a) is an example of dissociation of a screw dislocation  $\mathbf{BA}$  into partials  $\mathbf{B\delta}$  (right) and  $\mathbf{\delta A}$  (left). They have strong and weak intensity peaks respectively. The two white arrows indicate contrasts due to the very short partials with the Burgers vectors  $\mathbf{A\delta}$  (left) and  $\mathbf{B\delta}$  (right). From the known orientation of the specimen and the diffraction vectors  $-\mathbf{g}, \mathbf{g}, 2\mathbf{g}, 3\mathbf{g}$ , it is possible to calculate the four exact  $\beta'$  functions involved in the Howie-Whelan equations [16,22]. They are derived analytically from the elastic displacement field of an ADPS described in §2. A number of about 22000 pixel intensities is required to build a computed image.

Figure 9(b) is a computed image for which the bottom free surface relaxation is taken into account. Among other computed images, figure 9(b) gives the best visual fit with the general experimental contrast. The corresponding geometrical parameters are :  $S = 1.5$  nm, which is for example the length MN of the shorter partial;  $L = 8.5 S$  ;  $\varepsilon = 2.5^\circ$ ; the local substrate thickness  $h = 2$  nm. Additional calculations show that when  $h$  increases from 2 nm to 5 nm, the contrast of the left partial  $\mathbf{\delta A}$  decreases rapidly with respect to the contrast of partial  $\mathbf{B\delta}$ . The screw dislocation segments  $\mathbf{\delta C}$  (and  $\mathbf{C\delta}$ ) are out of contrast, which is expected from the invisibility rule [16]. Figure 9(c) give another image computed with the same parameters as figure 9(b) except that the elastic field used considers the medium as infinite. This image presents no visible contrast of the left partial  $\mathbf{\delta A}$ . On the other hand, in figures 9(b) and 9(c), the contrasts of the corresponding top dislocation branches are sensibly different. Figures 9(d,e) are intensity profiles across dislocation  $\mathbf{BA}$  for  $X_3 = -40$  nm. These profiles correspond to the bottoms of the images 9(b,c) respectively. The comparison of these theoretical profiles confirms that the left peak intensity is sensitive to free surface relaxation. In figure 9(d), the calculated peak intensities  $I$  of the two vertical partials  $\mathbf{\delta A}$  and  $\mathbf{B\delta}$  are noticeable and in reasonable agreement with the contrasts near the bottom of figure 9(a). The theoretical positions of the dislocation cores, indicated by the two small vertical bars (spacing

theoretically close to 4 nm) near the origin of the abscissa axes, are not far from the theoretical intensity peaks.

The theoretical treatment of the strain contrast applied to construct figure 9(b) assumes a semi-infinite medium and a dark field image formed from a weak Bragg reflection. A more exact treatment of the strain around the dissociated node, which would take account of both free surfaces being free of forces, has not been considered in the present work because it is still an unsolved problem. Note, however, that the simpler problem of a straight dissociated  $60^\circ$  dislocation in an ultrathin silicon foil has been discussed recently by two of the present authors [23]. As shown in [15-17], since only the planes very close to the dislocation core are sufficiently tilted to come into the Bragg position [15-17], it is reasonable to think that the strain contrast due to the layer side (thickness = 25 nm) is quite negligible compared with that of the substrate when  $h$  is close to 2 nm.

#### 4. Conclusions.

A compact expression of the elastic displacement field of a sharply angular dislocation parallel and close to a free surface has been obtained from the combination of previous works on angular dislocations [2-4] and further simplifications. The validity and convenience of this expression has been verified by a dark-field TEM study of a (111)Si low angle twist boundary with  $\psi = 0.16^\circ$ . The analysis of the dislocation network by a  $\mathbf{g}(3\mathbf{g})$  diffraction mode confirms a finding of ref. [9], obtained for a twist angle  $\psi \approx 0.4^\circ$  from qualitative weak-beam investigation, namely that the small dissociated nodes are of extrinsic type. No interfacial precipitates were found in our specimen, nor were double-ribbons of stacking faults. For our specimen, the intrinsic/extrinsic junctions are very narrow and give rise to very short screw partial dislocations with lengths as close as 1.5 nm. Finally, from the comparison between the experimental image of an extrinsic node and numerous computed images, we conclude that some contrasts of partial dislocations can be sensitive to a nearby free surface if dislocations are placed at a few nanometers from the surface.

#### Captions of figures

Figure 1

Description of dislocations for which the elastic displacement fields are algebraical.  $\mathbf{N}$  is the normal to the plane of the free surface. The “Yoffe” dislocation has a Burgers vector  $\mathbf{b}_1$ , while the “Comninou” dislocation has the Burgers vector  $\mathbf{b}_2$ . The angle  $\beta$  is less or equal to  $\pi/2$ . The line orientations are indicated by the black arrows.

Figure 2

The elastic field of a sharply angular dislocation oriented TOQ, parallel to the free surface, is obtained from the superposition of two Comninou dislocations oriented TOU (Burgers vector **b**) and QOU (Burgers vector **-b**) with  $\beta$  angles equal to  $\pi/2$ .

Figure 3

Schematic diagram of the cross section of the thin bicrystalline foil. The normal **N** is directed towards the screen side of the microscope. The free surface is therefore on the substrate side where *h* is a few nanometers. The hexagonal dislocation network is extended along the (111) plane. The substrate thickness *h* can go to zero near the edge of the foil.

Figure 4

Many-beam bright field image of the low angle twist boundary. Misorientation  $\psi = 0.18^\circ$ . Image formed with the transmitted beam pointed by a black oval in the diffraction pattern. The electron beam is very close to **B** = [111]. The white arrows indicate two close and different dissociated nodes.

Figure 5

Dark-field image of the low angle twist boundary. Image taken with the beam **g** encircled by the black oval in the inserted diffraction pattern and the **g**(3**g**) diffracting mode. The electron beam is close to **B** = [855]. The horizontal segments of screw dislocations appears clearly dissociated.

Figure 6

Schematic diagram of the partial dislocations forming an extrinsic node of the dislocation network. The truncated triangle corresponds, for instance, to the node at the left hand side of the white arrow in figure 4.

Figure 7

Model describing the elastic field generated by an extrinsic node, in terms of 12 superposed angular dislocations parallel to the surface. The geometry of the dislocation lines is represented in projection on the screen relative to the axis system  $OX_1X_2X_3$ .

Figure 8

Dark-field image of the low angle twist boundary. Image taken with the indicated **g** diffraction vector and the **g**(3**g**) diffracting mode, in a region where the substrate thickness goes to zero. The electron beam is close to **B** = [558].

Figure 9

Comparison between the experimental contrast of an extrinsic node and calculated images. (a) **g**(3**g**) dark-field image taken with an electron beam very close to **B** = [558]. Calculated images assuming dislocation lines as described in figure 6 : (b) with and (c) without free surface elastic relaxation. (d,e) Respective calculated intensity profiles at  $X_3 = -40$  nm.

## References

- [1] P. P. Groves and D. J. Bacon, *Phil. Mag.* 22 (1970) p.83.
- [2] E. Yoffe, *Phil. Mag.* 5 (1960) p.161.
- [3] E. Yoffe, *Phil. Mag.* 6 (1961) p.1147.
- [4] M. Comninou and J. Dundurs, *J. Elasticity* 5 (1975) p.203.
- [5] R. Bonnet, S. Youssef, S. Neily, A. K. Gutakovskii, *C. R. Phys.* 6 (2008) p.34.
- [6] F. Fournel, H. Moriceau, N. Magnea, J. Eymery, J.-L. Rouvière, K. Rousseau, B. Aspar, *Mat. Sc. Eng. B73* (2000) p.42.
- [7] F. Fournel, K. Rousseau, H. Moriceau, J. Eymery, J.-L. Rouvière, N. Magnea, B. Aspar, *Appl. Phys. Lett.* 80 (2002) p.793.
- [8] M. Dynna, J. L. Vassent, A. Marty and B. Gilles, *J. Appl. Phys.* 80 (1996) p.2650.
- [9] J. P. Hirth, J. Lothe, *Theory of dislocations* (2d ed., John Wiley and Sons, New York 1982), p. 60 and 837.
- [10] H. Föll, C. B. Carter, *Phil. Mag. A*, 40 (1979) p.497.
- [11] P. C. J. Gallagher, *Phys. Stat. Sol.* 16 (1966) p.95.
- [12] A. G. Cullis, *J. Microsc.* 98 (1973) p.191.
- [13] M. Schmid, A. Biedermann, H. Sandler, P. Varga, *Phys. Rev. Lett.* 69 (1992) p.925.
- [14] R. Bonnet, *Phys. Rev.* 61 (2000) p.14059.
- [15] D. J. H. Cockayne, I. L. F. Ray, M. J. Whelan, *Phil. Mag.* 20 (1969) p.1265.
- [16] P. Hirsch, A. Howie, R. B. Nicholson, D. W. Pashley, M. J. Whelan, in *Electron Microscopy of Thin Crystals*, 2d ed. (Krieger, Malabar, FL, USA, 1977) p. 289.
- [17] B. William and C. Barry Carter, *Transmission Electron Microscopy. III Imaging*, Plenum Press, New York, 1996, p. 413.
- [18] A.K. Head, P. Humble, L.M. Clarebrough, A.J. Morton, C.T. Forwood, *Computed Electron Micrographs and Defects Identification*, North-Holland, Amsterdam, 1973.
- [19] R. Bonnet, M. Loubradou, S. Youssef, J.-L. Rouvière, F. Fournel, *Phil. Mag.* 89 (2009) p.413 .

[20] N. Thompson, Proc. Phys. Soc. B 66 (1953) p. 481.

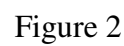
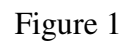
[21] B. D. Cullity, Elements of X-ray diffraction (Addison-Wesley Pub. Cy., 3d ed., Reading, MA, USA, 1967) p. 484.

[22] A. Howie, M. J. Whelan, Proc. R. Soc. A 263 (1961) p.217.

[23] S. Youssef, R. Bonnet, Phil. Mag. 87 (2007) p. 4935.

Acknowledgments : The authors thank Dr V. Poydenot for the delicate preparation of the specimens and Dr D. H. Warrington for his pertinent remarks on the manuscript.

David, here you can read something in red  
to help more visible  
corrections



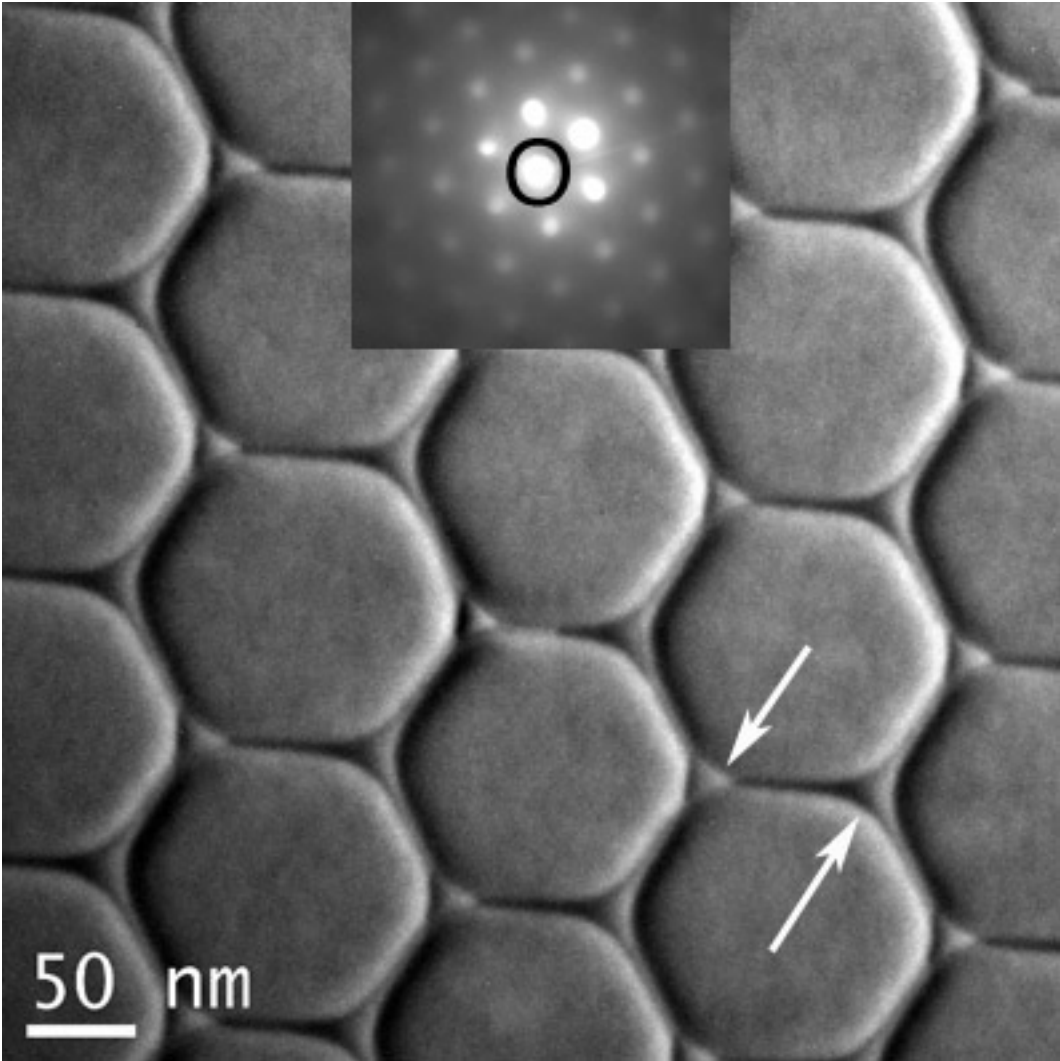


Figure 4



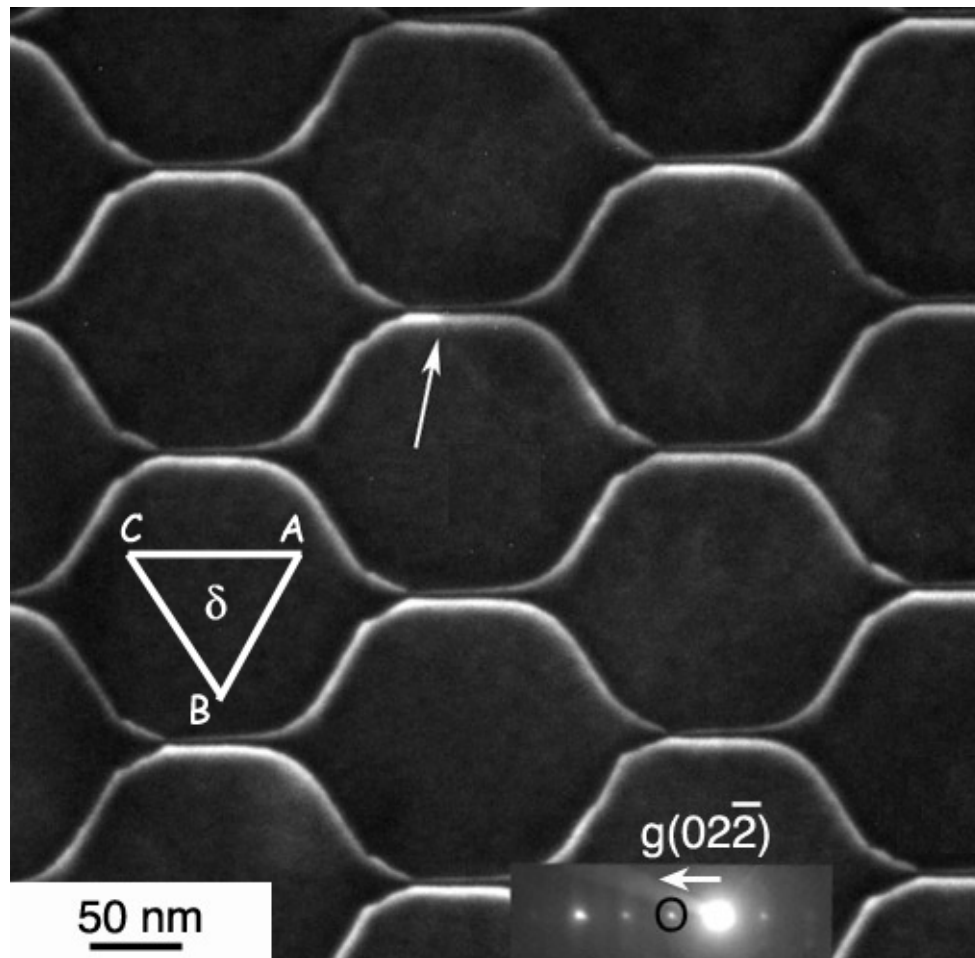


Figure 5



1  
2  
3  
4  
5  
6  
7  
8  
9  
10  
11  
12  
13  
14  
15  
16  
17  
18  
19  
20  
21  
22  
23  
24  
25  
26  
27  
28  
29  
30  
31  
32  
33  
34  
35  
36  
37  
38  
39  
40  
41  
42  
43  
44  
45  
46  
47  
48  
49  
50  
51  
52  
53  
54  
55  
56  
57  
58  
59  
60

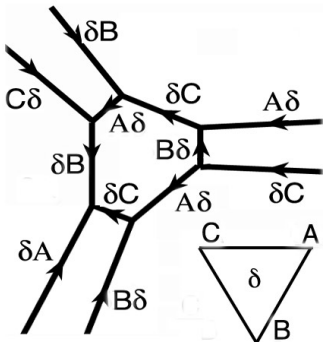


Figure 6

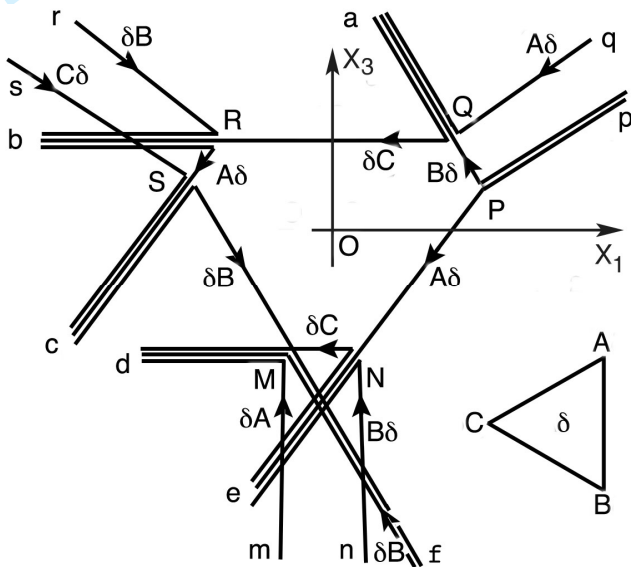


Figure 7

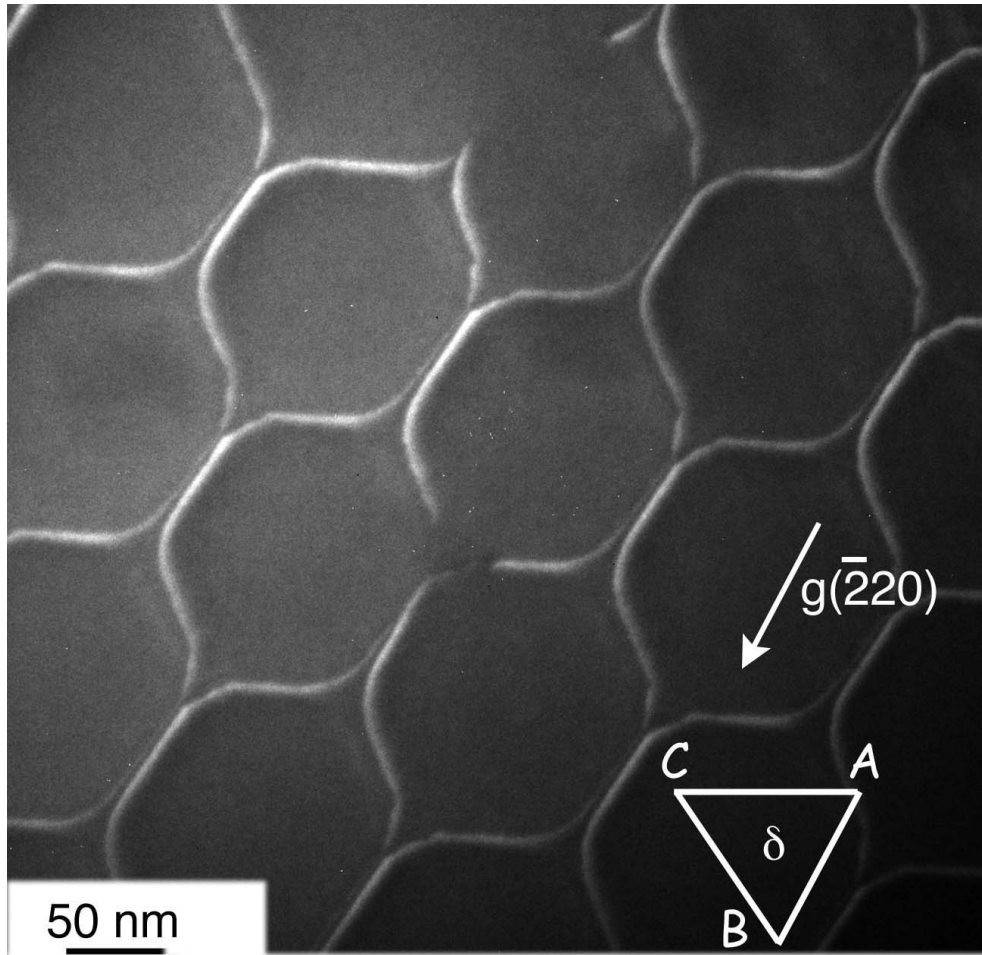


Figure 8

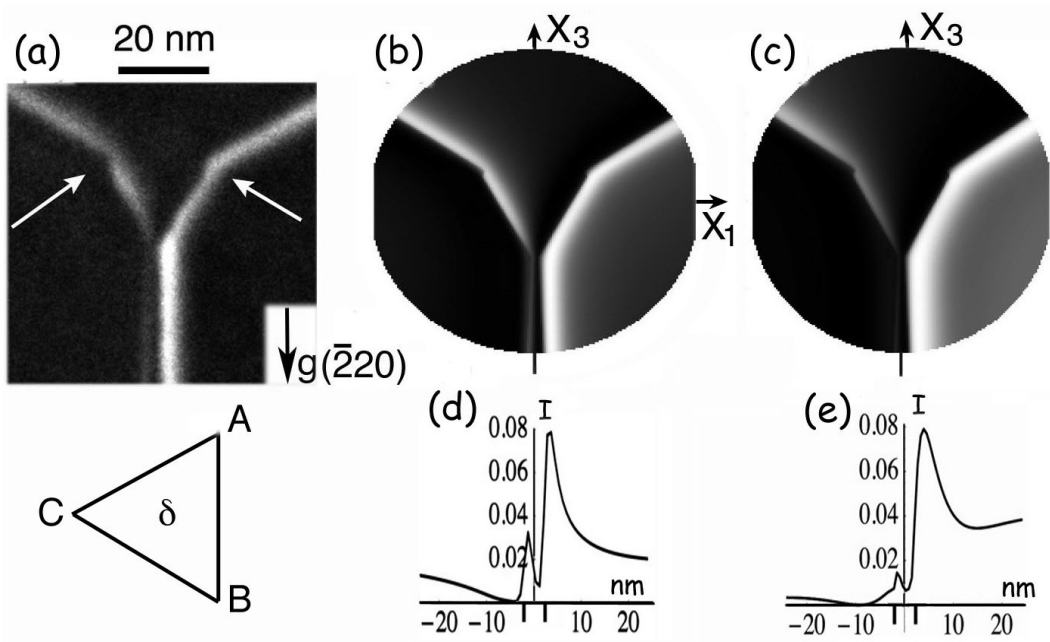


Figure 9